Lateral Spin Valve Based on the Two-Dimensional CrN/P/CrN Heterostructure

M. Modarresi,[1] A. Mogulkoc,[2,*] Y. Mogulkoc,[3] and A.N. Rudenko[4,5,6]

[1] *Department of Physics, Ferdowsi University of Mashhad, 9177948974 Mashhad, Iran*

[2] *Department of Physics, Faculty of Sciences, Ankara University, 06100 Tandogan, Ankara, Turkey*

[3] *Department of Engineering Physics, Faculty of Engineering, Ankara University, 06100 Tandogan, Ankara, Turkey*

[4] *School of Physics and Technology, Wuhan University, Wuhan, 430072, China*

[5] *Radboud University, Institute for Molecules and Materials, Heyendaalseweg 135, 6525 AJ Nijmegen, Netherlands*

[6] *Theoretical Physics and Applied Mathematics Department, Ural Federal University, 620002 Ekaterinburg, Russia*

(Received 29 January 2019; revised manuscript received 8 April 2019; published 7 June 2019)

We propose a spin valve based on a blue-phosphorus monolayer sandwiched between two half-metallic two-dimensional CrN layers. We use density-functional theory combined with Boltzmann transport theory to investigate both the structural and the magnetic stability of the CrN/P/CrN heterostructure and to study its spin-dependent transport properties. Among the different possible layer stackings considered, only one is shown to be thermodynamically stable, corresponding to the *AA* stacking. In this geometry, the critical temperature of magnetic ordering is estimated to be around 150 K. The electronic structure of CrN/P/CrN is strongly dependent on the mutual orientation of the magnetic moments in individual CrN layers. If the alignment is parallel, only one spin channel predominantly contributes to the electronic bands in the vicinity of the Fermi energy. In the case of an antiparallel alignment, both spin channels contribute to the electronic states. The alteration of magnetic moments affects electronic transport, causing magnetoresistance of up to 12% at moderate dopings.

DOI: 10.1103/PhysRevApplied.11.064015

I. INTRODUCTION

A spin-valve device usually consists of two ferromagnetic (FM) thin films separated by a nonmagnetic spacer. The electron-transport properties of such a device depend on the relative orientation of magnetization in the individual FM layers. For current passing perpendicular to the FM layers, the majority-spin states are conductive, while the minority-spin electrons are reflected or spin-flip scattered due to the lack of empty electronic states. As a result, if the magnetic alignment of magnetic layers is parallel, the total conductivity through the device is mostly determined by the spin-up channel. In contrast, in the case of the antiparallel alignment of FM layers, the conductivity is suppressed by one of the magnets, resulting in zero or small net current [1]. Spin valves have found application in information storage, logical devices, and magnetic sensors [2–10].

With the emergence of two-dimensional (2D) materials, they are being proposed as building blocks for spin-valve devices. Recently, some vertical spin valves based on thin FM layers and 2D spacers were fabricated [2,11–17]. Another milestone in the field was set by the discovery of 2D ferromagnets [18]. CrI_3 was the first magnetic 2D material, with a Curie temperature of 45 K [19]. Remarkably, the magnetic properties of the 2D phase of CrI_3 can be controlled electrically [20], which is of great interest for applications [21]. Van der Waals spin valves based on bilayer graphene and two CrI_3 monolayers were proposed. It was shown that the relative orientation of the magnetic moments in CrI_3 has a strong impact on the conductivity [22]. Experimentally, high magnetoresistance is observed for CrI_3 sandwiched between graphite [23] and graphene [24,25] contacts, forming a magnetic tunnel junction.

Theoretically, ferromagnetism has been proposed in many 2D materials, including graphene-based *sp* materials [26,27]. Nevertheless, conventional transition-metal compounds appear to be more suitable in practice, mainly because of their thermal stability [28]. CrN is a new member of the family of 2D ferromagnets with half-metallicity and presumably high Curie temperatures. A robust half-metallic FM phase was predicted for the rock-salt [29] and hexagonal [30] structures of the CrN monolayer. Half-metallicity is especially important in the context of spin valves, as it allows 100% spin filtering to be achieved.

*mogulkoc@science.ankara.edu.tr

CrN-based spin valves have not yet been reported in the literature.

Motivated by the above observations, here we study the electronic, magnetic, and transport properties of a CrN-based spin valve. We consider two hexagonal CrN monolayers separated by a blue-phosphorus insulating spacer, which is perfectly commensurate with the CrN structure. Blue phosphorus is a hexagonal (A7 phase) counterpart of orthorhombic (A17 phase) black phosphorus with similar stability [31,32]. Several techniques for fabricating blue phosphorus have been proposed, including epitaxial growth on metallic (Au, Cu) and semiconducting (GaN) substrates [33–35]. In the present study, we first use density-functional theory (DFT) to investigate both the structural and the magnetic stability of the CrN/P interface. We then analyze its electronic properties and study the spin-dependent transport properties of the CrN/P/CrN heterostructure by means of Boltzmann transport theory. We find the most-favorable stacking pattern and determine its Curie temperature within the random-phase approximation, which is estimated to be around 150 K. The transport properties of CrN/P/CrN are found to be strongly dependent on doping, as well as on the mutual orientation of magnetization in the individual CrN layers, with a resulting magnetoresistance of up to 12%.

This paper is organized as follows. In Sec. II, we present the computational method and details of our calculations. In Sec. IIIA, we discuss the electronic properties and magnetic stability of individual CrN layers. Section IIIB describes the CrN/P interface, including its dynamical stability. Electronic properties and magnetic stability of the CrN/P/CrN heterostructure are discussed in Sec. IIIC, while its spin-dependent transport properties are presented in Sec. IIID. In Sec. IV, we briefly summarize our results and conclude the paper.

II. COMPUTATIONAL METHODS

The first-principles electronic structure calculations performed in this study are based on DFT. The projected-augmented-wave method [36,37] is used as implemented in the Vienna *ab initio* simulation package (VASP) [38,39]. A plane-wave basis set with a kinetic energy cutoff of 800 eV is considered in all first-principles calculations. The exchange and correlation effects are described by means of the generalized-gradient approximation with the Perdew-Burke-Ernzerhof functional [40]. To capture the effects of strong electronic correlations, we use the DFT with Hubbard U parameter (DFT + U) method [41,42], applying the effective on-site Coulomb repulsion to the d orbitals of Cr atoms. If not mentioned otherwise, we use $U = 3$ eV, which is the value reported for a CrN monolayer [30]. Numerical integration over the Brillouin zone is performed with the Monkhorst-Pack scheme [43] with a $32 \times 32 \times 1$ **k**-point mesh. The atomic positions and lattice constants are both relaxed with use of the conjugate-gradient method to reach the minimum-energy configuration as a ground state. In the relaxed structure, the maximum Hellmann-Feynman force acting on each atom is less than 0.001 eV/Å. The convergence criterion for total energy minimization is set to 10^{-8} eV between two sequential steps. To avoid interaction between periodic unit-cell images, we use a 30-Å vacuum perpendicular to the 2D plane. To take into account the van der Waals interactions between weakly bound 2D layers, we use the DFT-D2 method [44]. For comparison, selective calculations performed in this work are repeated using different exchange-correlation functionals. Namely, we use the local-density approximation and nonlocal van der Waals correction to dispersion forces [45,46] to reproduce the main results of the present work. We find that our results remain essentially the same with respect to different approximations for exchange and correlation effects (see Supplemental Material for details [47]).

For the relaxed heterostructures, we calculate the interface binding energy defined as

$$E_b = E^N - \sum_{i=1}^{N} E_i, \tag{1}$$

where E^N is the energy of the heterostructure composed of N layers, and E_i is the energy of ith separated layer. To examine the dynamical stability of relaxed structures, the phonon spectra are calculated with density-functional perturbation theory with use of the PHONOPY code [48].

Electronic transport properties are calculated within the semiclassical Boltzmann transport theory with use of the BOLTZWANN code [49] in conjunction with the WANNIER90 code [50] used to interpolate the band structure by means of the maximally localized Wannier functions [51,52]. The electrical conductivity along the i direction is calculated as follows:

$$\sigma_{ii}(\mu, T) = e^2 \int_{-\infty}^{+\infty} d\varepsilon \left(-\frac{\partial f(\varepsilon, \mu, T)}{\partial \varepsilon}\right) \Sigma_{ii}(\varepsilon), \tag{2}$$

where $f(\varepsilon, \mu, T)$ is the Fermi-Dirac distribution function

$$f(\varepsilon, \mu, T) = \frac{1}{e^{(\varepsilon-\mu)/k_B T} + 1}, \tag{3}$$

and $\Sigma_{ij}(\varepsilon)$ is the transport distribution function

$$\Sigma_{ij}(\varepsilon) = \frac{1}{V} \sum_{n,\mathbf{k}} v_i(n, \mathbf{k})\, v_j(n, \mathbf{k})\, \tau(n, \mathbf{k})\, \delta\left(\varepsilon - \varepsilon_{n,\mathbf{k}}\right), \tag{4}$$

where $\varepsilon_{n,\mathbf{k}}$ is the energy of the nth band at wave vector $\mathbf{k}$, $v_{i(j)}(n, \mathbf{k})$ is the ith (j th) component of the group velocity,

V is the unit-cell volume, and τ is the relaxation time. In all transport calculations, the relaxation-time approximation is used, with the constant relaxation time set to $\tau = 10$ fs, and room temperature, $T = 300$ K, is used. For 2D structures the unit-cell volume is ill-defined due to the vacuum size along the z axis. For comparison, we normalize the conductivity to the effective slab thickness, which is 1.4 Å for monolayer CrN and 8.16 Å for trilayer CrN/P/CrN.

The interaction between the spins is modeled according to the classical Heisenberg Hamiltonian:

$$H = \sum_{i,j} J_{ij}\,\mathbf{S}_i \cdot \mathbf{S}_j + \sum_i A_i (\mathbf{S}_i \cdot \mathbf{z}_i)^2, \tag{5}$$

where $J_{ij} \equiv J(\mathbf{R}_{ij})$ is the exchange interaction between spins $\mathbf{S}_i$ and $\mathbf{S}_j$, A_i is the single-ion anisotropy at spin $\mathbf{S}_i$, and $\mathbf{z}_i$ is the unit vector pointing in the direction of the easy-magnetization axis. The second term on the right in Eq. (5) is crucially important for the stabilization of magnetic order in two dimensions [53,54]. To investigate the thermal stability of magnetic order, we estimate the Curie temperature T_C for monolayer CrN and its heterostructures. Following Refs. [55,56], we use the random-phase approximation to estimate the Curie temperature within the Heisenberg Hamiltonian. In the simplest case of a single sublattice and FM ground state, the corresponding expression is

$$k_B T_C = \frac{2}{3}\frac{S+1}{S}\left(\frac{1}{\Omega}\int d\mathbf{q}\, N^{-1}(\mathbf{q})\right)^{-1}, \tag{6}$$

where $\Omega = 4\pi/\sqrt{3}a^2$ is the Brillouin-zone area and $N(\mathbf{q}) = \Delta + J(0) - J(\mathbf{q})$ is the spin-wave energy, with $J(\mathbf{q})$ being the Fourier transform of $J(\mathbf{R}_{ij})$, and $\Delta = AS^2$ is the magnetocrystalline anisotropy. By expanding the spin-wave energy up to the second order in q, that is, $\Delta + J(0) - J(\mathbf{q}) \to \Delta + \frac{3}{2}q^2a^2J$, and assuming that the Brillouin zone has a circular shape, we arrive at the following formula for the Curie temperature:

$$k_B T_C = \frac{4\sqrt{3}}{3}\frac{S+1}{S}\frac{JS^2}{\ln\left(\frac{\Delta+\sqrt{3}JS^2}{\Delta}\right)}, \tag{7}$$

which is applicable to hexagonal single-sublattice 2D ferromagnets.

III. RESULTS AND DISCUSSION

A. Electronic properties and magnetic stability of monolayer CrN

Monolayer CrN has a hexagonal crystal structure (point group C_{3v}) with the relaxed lattice constant $a = 3.26$ Å, and a negligible buckling, which can be ignored as it has a vanishing effect on the electronic structure.

We first consider the electronic and magnetic properties of isolated monolayer CrN. Its ground state is FM with the magnetic moments $M = 3.0\mu_B$ localized on Cr atoms, which corresponds to spin $S = 3/2$. To estimate the magnetic stability, we determine the exchange interactions defined in terms of the Heisenberg Hamiltonian [Eq. (5)] with only nearest-neighbor interactions taken into account. To this end, we calculate the total energies of two distinct magnetic configurations: collinear FM and noncollinear 120° Néel states (see the insets in Fig. 1 for spin distributions). In both cases the lattice symmetry remains unchanged.

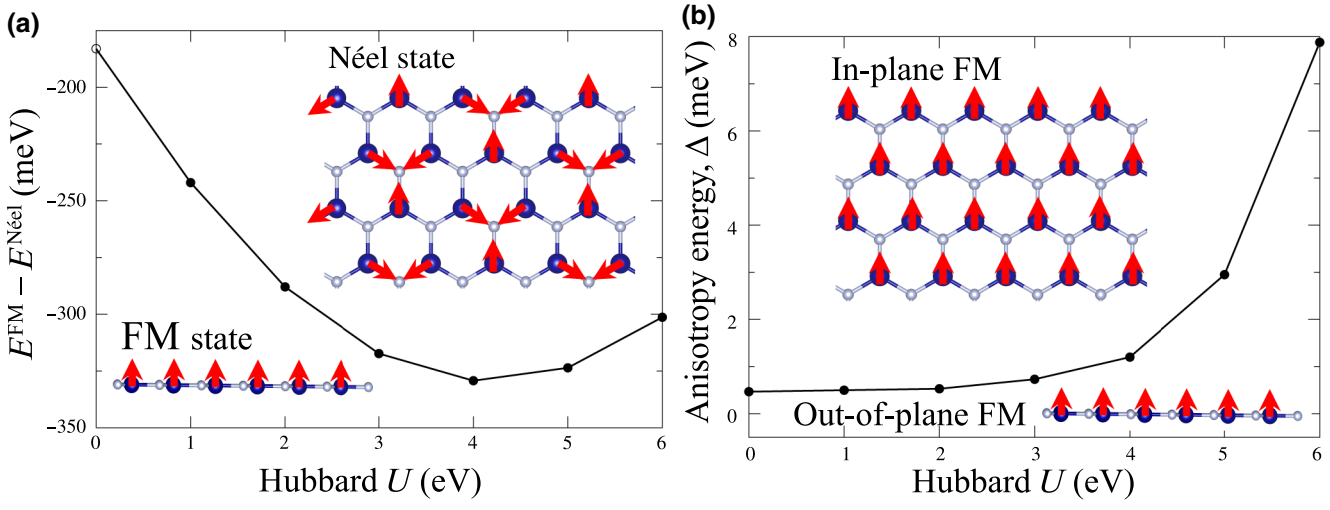

FIG. 1. (a) Energy difference between the FM and Néel states in single-layer CrN calculated per Cr atom as a function of the Hubbard U parameter. (b) The magnetic anisotropy energy (Δ) calculated per Cr atom as the difference between the out-of-plane and in-plane FM configurations in single-layer CrN for a series of Hubbard U parameters. The insets show the alignment of spins for the different magnetic configurations.

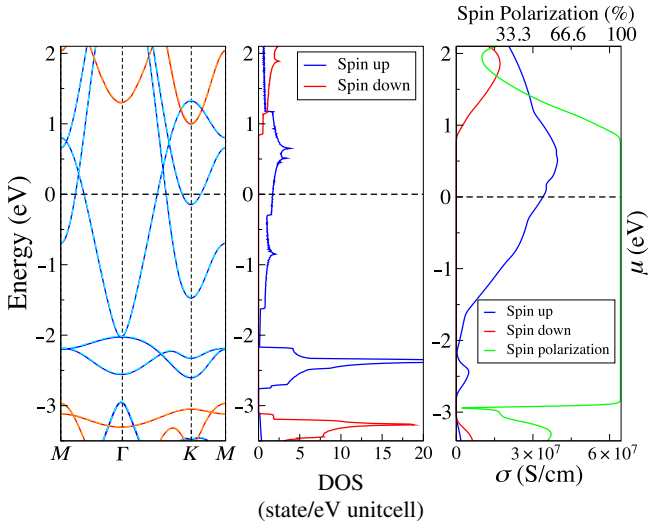

FIG. 2. (a) Electronic bands calculated for spin-up (blue line) and spin-down (red line) states of monolayer CrN. The dashed lines are the DFT bands, while the solid lines are the Wannier-interpolated bands. (b) The corresponding spin-resolved DOS. (c) Spin-up ($\sigma^{\uparrow}$) and spin-down ($\sigma^{\downarrow}$) components of the lateral conductivity, as well as its spin polarization [Eq. (8)] calculated as a function of the chemical potential μ.

The exchange energy for the FM configuration is $E^{\mathrm{FM}} = 12JS^2$ per atom, while for the Néel state it is $E^{\mathrm{Néel}} = -6JS^2$. The exchange-interaction strength can, therefore, be calculated as $J = (E^{\mathrm{FM}} - E^{\mathrm{Néel}})/18S^2$. In Fig. 1(a), we show the absolute energy difference between the FM and Néel states as a function of the Hubbard U parameter. For $U = 3$ eV, which corresponds to the case of pristine CrN, we obtain $J^{U=3} \approx 7.83$ meV, which is close to the value reported for the rock-salt structure of monolayer CrN [29]. In the presence of a dielectric substrate, the on-site Coulomb interaction on Cr atoms would be screened, leading to smaller U values. In the limit of large screening ($U = 0$), the exchange interaction is suppressed considerably, yielding $J^{U=0} \approx 4.52$ meV. As a next step, we calculate the magnetic anisotropy energy Δ as the energy difference between the magnetic configuration with in-plane and out-of-plane spin alignments, $\Delta = E^{\mathrm{in}} - E^{\mathrm{out}}$. We find that the easy-magnetization axis corresponds to the out-of-plane configuration. In Fig. 1(b), we show the calculated $\Delta(U)$ dependence. For pristine CrN ($U = 3$ eV), we obtain $\Delta^{U=3} \approx 0.73$ meV, while at $U = 0$, one has $\Delta^{U=0} \approx 0.47$ meV. As in the case of exchange interactions, the screening suppresses the anisotropy. We can now estimate the Curie temperature, which is $T_C^{U=3} = 209$ K and $T_C^{U=0} = 124$ K for the two situations considered. In both cases, the critical temperature lies well above the liquid-nitrogen temperature. It is worth noting that we obtain similar critical temperatures with different exchange-correlation functionals [47].

We now turn to the ground-state electronic properties of monolayer CrN. Figure 2(a) shows the band structure calculated in the vicinity of the Fermi energy, which demonstrates half-metal character, and the splitting between spin-up and spin-down states, being the origin of magnetism in CrN. The spin-up electronic bands are finite, while there is an approximately-4.0-eV energy gap for spin-down states, as can be seen from Figs. 2(a) and 2(b). This results are compatible with the data reported in Ref. [30]. In Fig. 2(c), we show spin-resolved lateral conductivity $\sigma^{\uparrow}$ ($\sigma^{\downarrow}$) of monolayer CrN as a function of the chemical potential μ. One can see that in a wide region around the neutrality point ($\mu = 0$), the conductivity is determined exclusively by the spin-up states. To characterize the asymmetry of spin-up and spin-down states with regard to the transport properties, we define the spin polarization of the conductivity as

$$\sigma_{\mathrm{SP}} = \frac{\sigma^{\uparrow} - \sigma^{\downarrow}}{\sigma^{\uparrow} + \sigma^{\downarrow}}. \tag{8}$$

For monolayer CrN, the spin polarization is 100% for any realistic doping regime, which indicates perfect spin filtering.

One of the possible ways to utilize the spin-filter effect is to manipulate the direction of magnetization of two or more FM layers, forming a heterostructure. A typical heterostructure is composed of conducting layers separated by an insulating spacer, coupled by weak van der Waals interactions. In what follows, we study the electronic and transport properties of the CrN/P/CrN heterostructure, composed of two hexagonal CrN monolayers and a blue-phosphorus monolayer. This system represents a minimal model for a CrN-based spin valve, schematically shown in Fig. 3. The choice of the spacer material is motivated by the small lattice mismatch between the lattices, which is less than 1%.

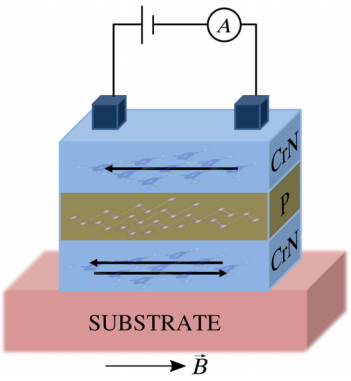

FIG. 3. A lateral spin-valve device based on 2D CrN ferromagnets separated by a phosphorus spacer. Arrows show the possible direction of magnetization controlled by an external magnetic field.

B. Thermodynamic stability of the CrN/P interface

We first investigate the energetic stability of the CrN/P interface. To this end, we consider two possible stacking patterns: *AA* and *AB*. Because of the buckling of both monolayers of CrN and P, there are two possible arrangements of atoms for each stacking pattern. For example, in the *AA* configuration, P atoms can be close to either Cr or N atoms of CrN. To determine the most-energetically-favorable geometry, we fully relax all four possible atomic configurations and compare their energies. The *AA* stacking in which P atoms are closer to Cr atoms [Figs. 4(d) and 4(e)] is found to be the stablest configuration, with a binding energy of 0.44 eV per cell. The energy difference between *AA* stacking and *AB* is 40 meV.

Besides the binding energies, we calculate the vibration spectrum to assess the dynamical stability of the *AA* and *AB* interfaces. In our calculations, we take only the magnetic ground state (FM) into account, but note the possibility of strong spin-lattice interactions in 2D magnets [58]. The corresponding phonon dispersion curves are shown in Fig. 4(a). Unlike monolayer P [31], there is no frequency gap between acoustic and optical phonon branches in the spectrum of monolayer CrN. As one can see, for the *AA* interface, all the phonon branches exhibit real frequencies, indicating dynamical stability of this configuration. Similarly to suspended monolayer CrN, the *AA* interface exhibits one quadratic out-of-plane mode [flexural acoustic (ZA)] and two linear in-plane modes (TA and LA) around the Γ point, which is typical of 2D systems. However, the interaction of CrN with P leads to a lowering of the vibration frequencies, especially for the LA mode. In contrast, three imaginary branches appear around the Γ and *M* points in the case of the *AB* interface. The imaginary frequencies indicate instability of the *AB* stacking and the tendency toward structural reconstruction. For this reason, we do not consider the *AB* interface in the following discussion.

Overall, the interaction between CrN and P preserves the FM ground state with spin-polarized electronic states. However, the hybridization between CrN and P orbitals affects the band structure. In Fig. 4(b), we show the electronic bands of the *AA*-stacked CrN/P bilayer. Both spin-up and spin-down bands cross the Fermi energy, meaning that both spin projections contribute to the Fermi surface properties, including conductivity. Nevertheless, the spin-up states remain the dominant contribution in the valence band. The corresponding partial density of states (DOS) is shown in Fig. 4(c), from which one can see that the CrN and P states hybridize in the vicinity of the Fermi energy.

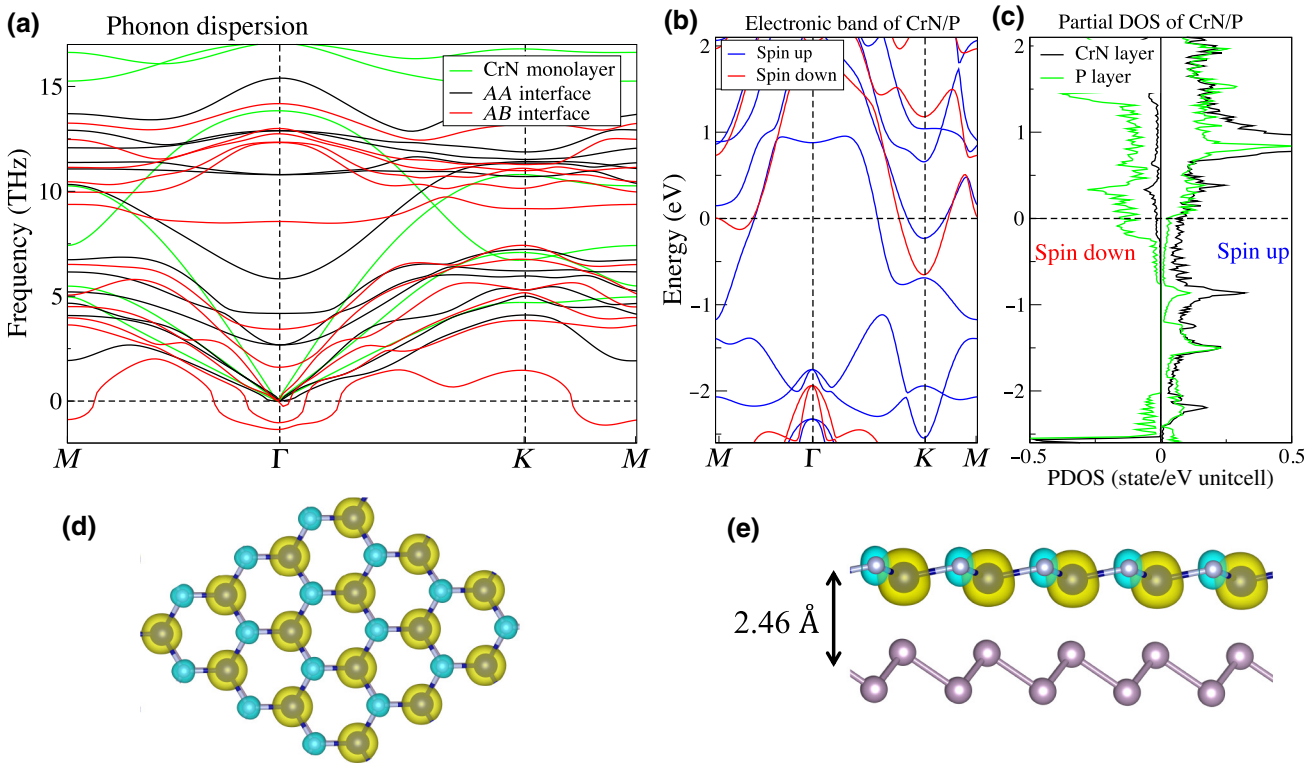

FIG. 4. (a) Phonon dispersion curves calculated for monolayer CrN, as well as for *AA* and *AB* stackings of CrN/P. (b) Spin-resolved electronic band structure. (c) Partial DOS (PDOS) for *AA* stacking of bilayer CrN/P. (d) Top view and (e) side view of the real-space spin-density distribution in CrN/P (*AA* stacking) created by means of VESTA [57]. Yellow and blue colors denote the direction of magnetization. The isosurface value is 0.03 $e/\text{Å}^3$.

TABLE I. Net magnetization per Cr atom (M), Heisenberg exchange interaction (J), on-site anisotropy energy (Δ), and the Curie temperature (T_C) estimated in this work for monolayer CrN, bilayer CrN/P, and trilayer CrN/P/CrN. The values for monolayer CrN are given for two different Hubbard U parameters. In the other cases, $U = 3$ eV is assumed.

System	M (μ_B)	J (meV)	Δ (meV)	T_C (K)
CrN ($U = 0$ eV)	3.00	4.52	0.47	124
CrN ($U = 3$ eV)	3.00	7.83	0.73	209
CrN/P	2.53	8.5	0.11	150
CrN/P/CrN	2.63[a]	8.13	0.12	146

[a]The value is given for the FM configuration. In the AFM case, $M = 0.16\mu_B$.

The DOS associated with P states is spin dependent, indicating that P atoms acquire a magnetic moment, estimated to be around $0.1\mu_B$. Moreover, the spin-down states at the neutrality point are mainly related to P states. The net magnetic moment in the CrN/P bilayer is reduced to $2.5\mu_B$ per cell compared with $3.0\mu_B$ in pristine CrN. Figures 4(d) and 4(e) shows top and side views of the corresponding real-space spin distribution, that is, $n^{\uparrow}(\mathbf{r}) - n^{\downarrow}(\mathbf{r})$, which is similar to the spin distribution of pristine monolayer CrN.

In CrN/P, the exchange interaction J is calculated to be approximately 8.5 meV, which is slightly larger than for pristine CrN in the absence of screening ($U = 3$ eV). On the other hand, the on-site anisotropy parameter Δ for bilayer CrN/P is significantly smaller, and is 0.11 meV. The difference in Δ between CrN and CrN/P suggests that the screening is not the only factor affecting the magnetic anisotropy, so the interface interaction between CrN and P has to be explicitly taken into account. In Table I, we summarize magnetism-related parameters for all the systems considered in this work.

C. Electronic properties and magnetic stability of the CrN/P/CrN heterostructure

To construct the van der Waals spin valve, we add a second CrN layer to the CrN/P system to form the CrN/P/CrN heterostructure. We use AA stacking for both the CrN/P interface and the P/CrN interface, taking into account their dynamical stability, and perform structural relaxation. A schematic atomic structure of CrN/P/CrN is shown in Figs. 6(a) and 6(b). Because of the buckling of the P layer, the interlayer distance between CrN and P is different for the two neighboring CrN layers, and is 2.46 and 3.10 Å. The calculated interface binding energy is about 0.64 eV per cell. To model two operating spin-valve states, we consider parallel (FM) and antiparallel [antiferromagnetic (AFM)] alignments of magnetic moments in the CrN layers, as shown in the insets in Fig. 5(a).

Figure 5(a) shows the energy difference between the corresponding FM and AFM configurations as a function of the Hubbard U parameter. Negative values indicate that the FM alignment is the ground state for all the U values. At $U = 3$ eV, the energy difference between the two states is 8.85 meV per Cr atom, which is a measure of the exchange interlayer coupling between the two CrN layers. Assuming nearest-neighbor coupling between Cr atoms belonging to different CrN layers, the interlayer exchange interaction can be estimated as $J_{\perp} \approx 1.97$ meV. However, this coupling does not directly affect the magnetic ordering in CrN/P/CrN as it is $\mathbf{q}$ independent, and thus does not modify the spin-wave spectrum [see Eq. (6)]. Therefore, the Curie temperature of the heterostructure is mainly determined by

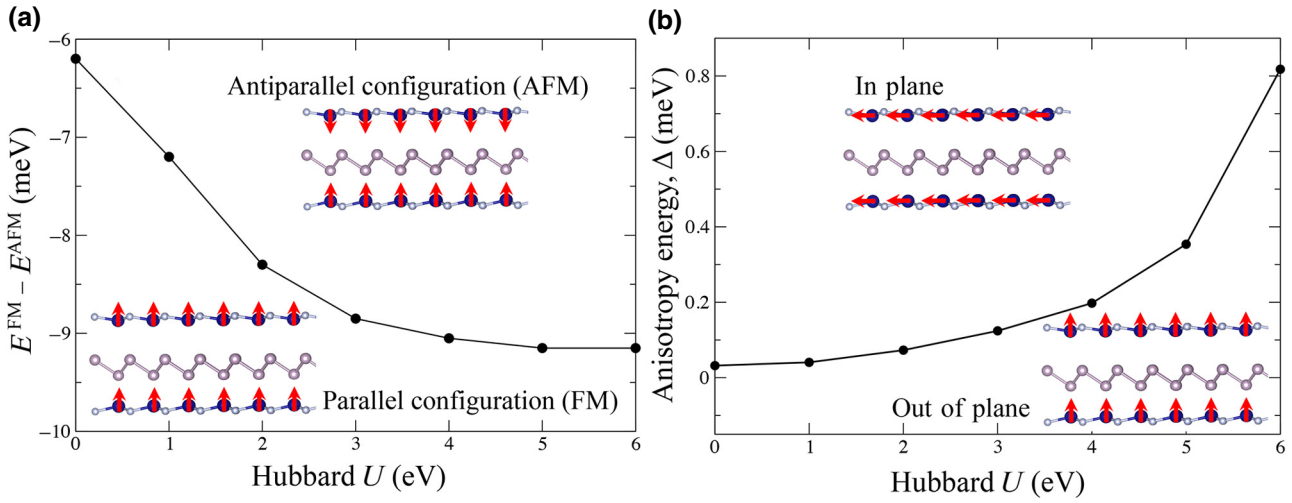

FIG. 5. (a) Energy difference between parallel (FM) and antiparallel (AFM) configurations in CrN/P/CrN calculated per Cr atom depending on the Hubbard U values. The insets show the spin distribution for both configurations. (b) The anisotropy energy ($\Delta = E^{in} - E^{out}$) per Cr atom.

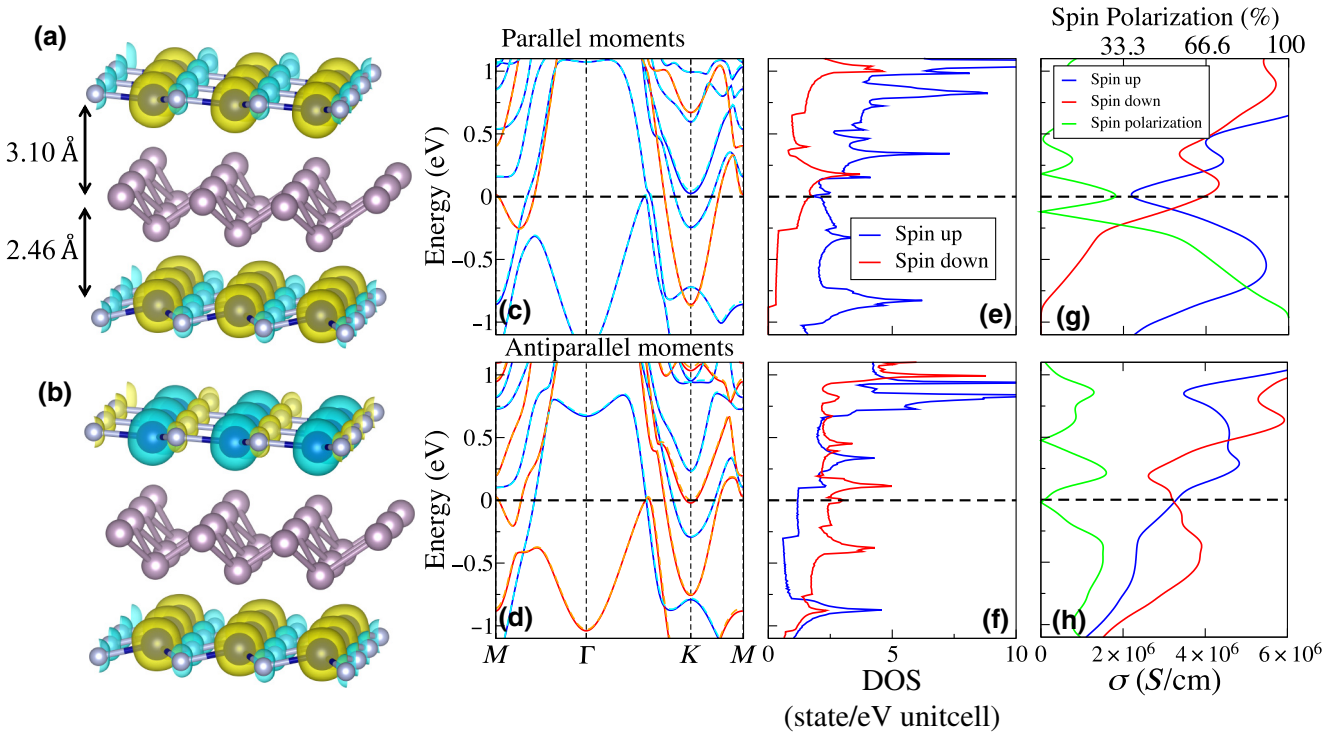

FIG. 6. Real-space distribution of magnetization calculated for (a) FM and (b) AFM configurations of CrN/P/CrN. The isosurface value for the magnetization is 0.03 $e/\text{Å}^3$. The corresponding spin-resolved electronic band structure and DOS are shown in (c)–(f), whereas (g),(h) show spin-dependent lateral conductivities as a function of the chemical potential.

the ordering of individual FM layers, whose mutual orientation could be controlled by the external magnetic field, as schematically shown in Fig. 3.

In the FM configuration, the total magnetic moment is $5.26\mu_B$ per formula unit. The magnetic moment on Cr atoms is $2.95\mu_B$ or $3.15\mu_B$, depending on the CrN layer. The difference is explained by the absence of mirror symmetry in CrN/P/CrN. Both N and P atoms acquire opposite magnetic moments, reducing the net magnetization. As can be seen from Table I, the net magnetization per CrN layer is nearly the same as in bilayer CrN/P. In the AFM configuration, there is a remaining magnetic moment of $0.33\mu_B$ per cell related to the different magnetization of CrN layers. The real-space spin distribution for the two configurations is shown in Figs. 6(a) and 6(b). For CrN/P/CrN, the calculated exchange coupling and magnetic anisotropy energy are 8.13 and 0.12 meV, respectively, which are comparable to those of bilayer CrN/P discussed earlier. The corresponding Curie temperature is estimated to be 146 K.

Figures 6(c)–6(f) show the spin-resolved band structure and DOS for parallel (FM) and antiparallel (AFM) alignments of magnetic moments of CrN layers. The electronic structure of the FM state [Figs. 6(c) and 6(e)] around the Fermi energy is similar to that of bilayer CrN/P. Although both spins contribute to the states around the Fermi energy, the main contribution is related to spin-up states. The situation is completely different for the AFM configuration [Figs. 6(d) and 6(f)]. Now the contributions of spin-up states and spin-down states to the electronic states are comparable in magnitude, which is expected to influence the transport properties.

D. Spin-dependent transport properties of CrN/P/CrN heterostructure

We now proceed to the transport properties of the CrN/P/CrN heterostructure. In Figs. 6(g) and 6(h), we plot spin-up ($\sigma^{\uparrow}$) and spin-down ($\sigma^{\downarrow}$) contributions to the lateral conductivity calculated for FM and AFM configurations. Besides, we show the spin polarization of the conductivity, as defined by Eq. (8). In the AFM case, the spin polarization is zero at the Fermi energy, where it reaches approximately 33% in the FM case. At positive energies, the behavior is similar for the two cases, while at negative energies the situation is different. Because of the absence of spin-down states in the FM configuration, the conductivity becomes strongly spin polarized, approaching 100% at −1 eV. On the other hand, in the AFM state the maximum spin polarization of approximately 30% is achieved at around −0.3 eV.

To further examine spin-dependent transport in CrN/P/CrN, we calculate the DOS projected onto different layers in the heterostructure, as shown in Figs. 7(a) and 7(b). In the FM configuration, the spin-down DOS for both CrN layers is zero or negligibly small around the Fermi

energy [Fig. 7(a)]. In this situation, the available spin-down states are mainly attributed to the P layer. The nonzero spin-up DOS implies that spin-up states are the main transport channel in ferromagnetic CrN/P/CrN. In contrast, in the case of the AFM alignment [Fig. 7(b)], the main transport channel in two oppositely magnetized CrN layers is different. One layer provides spin-up states, while the other layer provides spin-down states for transport. At the same time, the P layer exhibits a similar DOS in the both FM configuration and the AFM configuration. Unlike vertical spin valves, where current is passing in the direction perpendicular to the layers, the spin filtering in lateral spin valves is less efficient. Indeed, both conducting layers almost equally contribute to the overall lateral current, as can be deduced from Figs. 7(a) and 7(b). Nevertheless, the layer contribution is different for FM and AFM states, meaning that the switching between the magnetic states can be used to control the conductivity.

To assess the spin-valve efficiency, we calculate the magnetoresistance of CrN/P/CrN. Magnetoresistance characterizes the variation of the resistivity with respect to the rotation of magnetization in the conducting layers; that is,

$$\rho_{\mathrm{MR}} = \frac{\rho^{\uparrow\uparrow} - \rho^{\uparrow\downarrow}}{\rho^{\uparrow\downarrow}}, \tag{9}$$

where $\rho^{\uparrow\uparrow}$ ($\rho^{\uparrow\downarrow}$) is the resistivity in the FM (AFM) state, defined as the inverse conductivity for both spin channels; that is, $\rho = 1/(\sigma^{\uparrow} + \sigma^{\downarrow})$. The resulting magnetoresistance in shown in Fig. 7(c) as a function of the chemical potential. One can see that at low dopings ($|\mu| <$ 0.2 eV) the magnetoresistance ranges from 0% to 12%. At high electron dopings ($\mu >$ 0.2 eV) the magnetoresistance reaches its maximum of 27%. The values obtained are an order of magnitude greater than those reported in pioneer experimental work on thin Fe/Cr/Fe films [59]. Although the absolute magnetoresistance is not high by modern standards, it exceeds experimentally reported values for spin valves based on 2D materials, including vertical graphene spin valves [2,12], NiFe/MoS_2/NiFe junctions [15], and NiFe/WS_2/Co [16] structures, where the magnetoresistance is about 1%. Apart from the reasonable magnetoresistance, the CrN-based spin valves studied in the present work can be constructed as lateral devices, which is advantageous in terms of the fabrication. Moreover, ferromagnetic CrN layers offer low coercivity, meaning that the proposed device can work at low operating fields.

The consideration presented above does not take into account spin relaxation, which may influence the performance of spin-valve devices due to spin-flip processes. The spin flip could be induced by spin-orbit interaction or by thermal fluctuations of magnetic moments. However, in the context of CrN/P/CrN, these processes appear to be irrelevant for the following reasons. At temperatures below the critical temperature, spin fluctuations in ferromagnetic materials are obviously small, and cannot contribute significantly to the spin-flip processes. On the other hand, the processes determined by the spin-orbit coupling are also weak in compounds based on 3*d* transition metals such as chromium. Indeed, the probability ratio of electron scattering with (τ_1^{-1}) and without (τ_0^{-1}) spin-flip processes is proportional to λ^2, where λ is the spin-orbit coupling strength. At the same time, $\lambda \sim (Z\alpha)^2$, where Z is the atomic number and $\alpha \approx 1/137$ is the fine-structure constant. Therefore, the role of spin-flip scattering can be

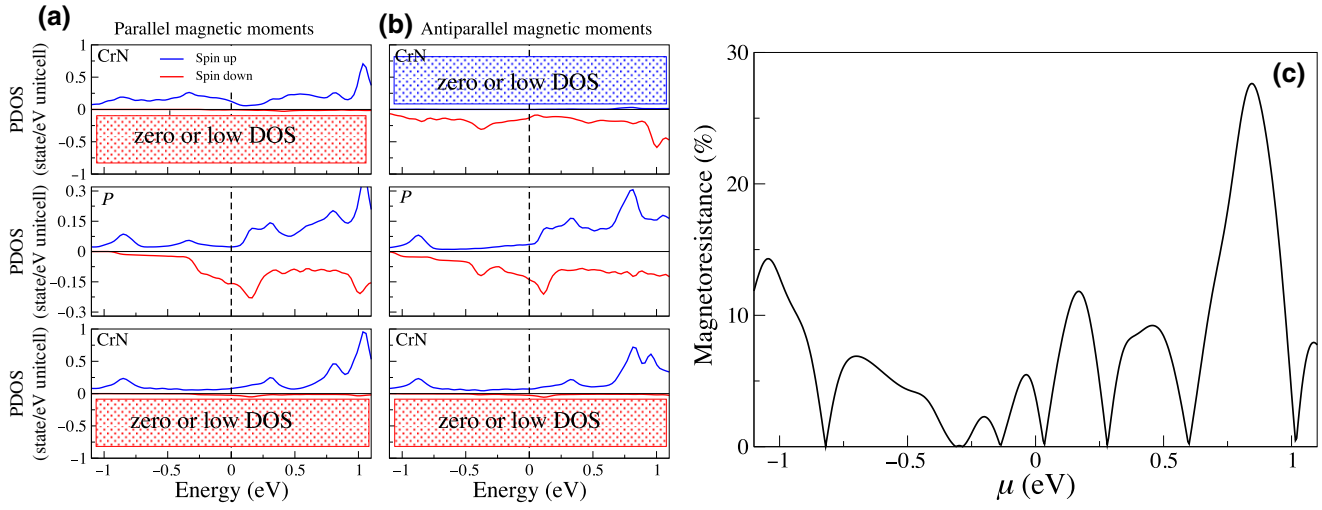

FIG. 7. Layer-resolved partial DOS (PDOS) calculated for CrN/P/CrN in the (a) parallel (FM) and (b) antiparallel (AFM) magnetic configurations. (c) Magnetoresistance in CrN/P/CrN calculated with Eq. (9) as a function of the chemical potential.

estimated from the ratio between spin-flip and transport scattering rates as $\tau_1^{-1}/\tau_0^{-1} \sim (Z\alpha)^4$ [60]. In the absence of heavy impurities, one can see that the spin-flip scattering rate is several orders of magnitude smaller than the transport scattering rate. This means that as long as the system remains conductive, spin-flip processes do not contribute significantly to spin-polarized current. Moreover, their effect could be further decreased by reducing the temperature or minimizing lateral dimensions of the sample. Finally, we note that real experimental conditions would include a number of factors (substrates, defects, leads, etc.), which are beyond our present consideration. We believe that our findings may stimulate further theoretical and experimental studies on this problem.

IV. CONCLUSION

In summary, we study the electronic and magnetic properties of a 2D CrN/P/CrN heterostructure using first-principles calculations. We determine the most-energetically-favorable CrN/P stacking configuration and analyze its phonon spectrum, which confirms dynamical stability of the interface. We calculate the exchange interactions and single-ion anisotropy parameters to estimate the Curie temperature within the random-phase approximation, which is found to be around 150 K for CrN/P/CrN. Transport properties are studied within Boltzmann transport theory by calculating spin-dependent electronic conductivities for different magnetic configurations (FM and AFM) of the system. The calculated magnetoresistance is around 12% in the low-doping regime. The combination of low coercivity of ferromagnetic CrN layers, relatively high operating temperatures, and reasonable magnetoresistance makes the CrN/P/CrN system an appealing candidate for a lateral spin-valve device.

ACKNOWLEDGMENTS

The authors acknowledge Ankara University for use of the high-performance computing facility through the AYP under Grant No. 17A0443001. A.N.R. acknowledges support from the FLAG-ERA JTC2017 Project "Gransport".

[1] E. Dagotto, in *Nanoscale Phase Separation and Colossal Magnetoresistance*. Springer Series in Solid-State Sciences, Vol. 136 (Springer, Berlin, Heidelberg, 2003).

[2] J. Meng, J.-J. Chen, Y. Yan, D.-P. Yu, and Z.-M. Liao, Vertical graphene spin valve with ohmic contacts, Nanoscale **5**, 8894 (2013).

[3] G. Li, S. Sun, R. J. Wilson, R. L. White, N. Pourmand, and S. X. Wang, Spin valve sensors for ultrasensitive detection of superparamagnetic nanoparticles for biological applications, Sens. Actuator A-Phys. **126**, 98 (2006).

[4] W. Qiu, L. Chang, Y.-C. Liang, J. Litvinov, J. Guo, Y.-T. Chen, B. Vu, K. Kourentzi, S. Xu, T. R. Lee, Y. Zu, R. C. Willson, and D. Litvinov, Spin-valve based magnetoresistive nanoparticle detector for applications in biosensing, Sens. Actuator A-Phys. **265**, 174 (2017).

[5] I. Žutić, J. Fabian, and S. Das Sarma, Spintronics: Fundamentals and applications, Rev. Mod. Phys. **76**, 323 (2004).

[6] W. Han, R. K. Kawakami, M. Gmitra, and J. Fabian, Graphene spintronics, Nat. Nanotech. **9**, 794 (2014).

[7] Z. Xiong, D. Wu, Z. V. Vardeny, and J. Shi, Giant magnetoresistance in organic spin-valves, Nature **427**, 821 (2004).

[8] S. Ikeda, J. Hayakawa, Y. Ashizawa, Y. M. Lee, K. Miura, H. Hasegawa, M. Tsunoda, F. Matsukura, and H. Ohno, Tunnel magnetoresistance of 604% at 300 K by suppression of Ta diffusion in CoFeB/MgO/CoFeB pseudo-spin-valves annealed at high temperature, Appl. Phys. Lett. **93**, 082508 (2008).

[9] E. W. Hill, A. K. Geim, K. Novoselov, F. Schedin, and P. Blake, Graphene spin valve devices, IEEE Trans. Magn. **42**, 2694 (2006).

[10] S. Cho, Y.-F. Chen, and M. S. Fuhrer, Gate-tunable graphene spin valve, Appl. Phys. Lett. **91**, 123105 (2007).

[11] M. Z. Iqbal, M. W. Iqbal, J. H. Lee, Y. S. Kim, S.-H. Chun, and J. Eom, Spin valve effect of NiFe/graphene/NiFe junctions, Nano Res. **6**, 373 (2013).

[12] S. Entani, H. Naramoto, and S. Sakai, Magnetotransport properties of a few-layer graphene-ferromagnetic metal junctions in vertical spin valve devices, J. Appl. Phys. **117**, 17A334 (2015).

[13] M. Z. Iqbal, G. Hussain, S. Siddique, and M. W. Iqbal, Interlayer reliant magnetotransport in graphene spin valve, J. Magn. Magn. Mat. **441**, 39 (2017).

[14] A. Avsar, J. Y. Tan, M. Kurpas, M. Gmitra, K. Watanabe, T. Taniguchi, J. Fabian, and B. Özyilmaz, Gate-tunable black phosphorus spin valve with nanosecond spin lifetimes, Nat. Phys. **13**, 888 (2017).

[15] W. Wang, A. Narayan, L. Tang, K. Dolui, Y. Liu, X. Yuan, Y. Jin, Y. Wu, I. Rungger, S. Sanvito, and F. Xiu, Spin-valve effect in NiFe/MoS2/NiFe junctions, Nano Lett. **15**, 5261 (2015).

[16] M. Z. Iqbal, M. W. Iqbal, S. Siddique, M. F. Khan, and S. M. Ramay, Room temperature spin valve effect in NiFe/WS_2/Co junctions, Sci. Rep. **6**, 21038 (2016).

[17] M. Z. Iqbal and G. Hussain, Electron spin dynamics in vertical magnetic junctions incorporating two-dimensional layered materials, J. Mater. Chem. C **5**, 11174 (2017).

[18] C. Gong and X. Zhang, Two-dimensional magnetic crystals and emergent heterostructure devices, Science **363**, eaav4450 (2019).

[19] B. Huang, G. Clark, E. Navarro-Moratalla, D. R. Klein, R. Cheng, K. L. Seyler, D. Zhong, E. Schmidgall, M. A. McGuire, D. H. Cobden, W. Yao, D. Xiao, P. Jarillo-Herrero, and X. Xu, Layer-dependent ferromagnetism in a van der Waals crystal down to the monolayer limit, Nature **546**, 270 (2017).

[20] S. Jiang, L. Li, Z. Wang, K. F. Mak, and J. Shan, Controlling magnetism in 2D CrI_3 by electrostatic doping, Nat. Nanotech. **13**, 549 (2018).

[21] B. Kiraly, A. N. Rudenko, W. M. J. van Weerdenburg, D. Wegner, M. I. Katsnelson, and A. A. Khajetoorians,

An orbitally derived single-atom magnetic memory, Nat. Commun. **9**, 3904 (2018).

[22] C. Cardoso, D. Soriano, N. A. Garcá-Martńez, and J. Fernández-Rossier, Van der Waals Spin Valves, Phys. Rev. Lett. **121**, 067701 (2018).

[23] D. R. Klein, D. MacNeill, J. L. Lado, D. Soriano, E. Navarro-Moratalla, K. Watanabe, T. Taniguchi, S. Manni, P. Canfield, J. Fernández-Rossier, and P. Jarillo-Herrero, Probing magnetism in 2D van der Waals crystalline insulators via electron tunneling, Science **360**, 1218 (2018).

[24] T. Song, X. Cai, M. W.-Y. Tu, X. Zhang, B. Huang, N. P. Wilson, K. L. Seyler, L. Zhu, T. Taniguchi, K. Watanabe, M. A. McGuire, D. H. Cobden, D. Xiao, W. Yao, and X. Xu, Giant tunneling magnetoresistance in spin-filter van der Waals heterostructures, Science **360**, 1214 (2018).

[25] Z. Wang, I. Gutiérrez-Lezama, N. Ubrig, M. Kroner, M. Gibertini, T. Taniguchi, K. Watanabe, A. Imamoglu, E. Giannini, and A. F. Morpurgo, Very large tunneling magnetoresistance in layered magnetic semiconductor CrI_3, Nat. Commun. **9**, 2516 (2018).

[26] J. Zhou, Q. Wang, Q. Sun, X. S. Chen, Y. Kawazoe, and P. Jena, Ferromagnetism in Semihydrogenated Graphene Sheet, Nano Lett. **9**, 3867 (2009).

[27] V. V. Mazurenko, A. N. Rudenko, S. A. Nikolaev, D. S. Medvedeva, A. I. Lichtenstein, and M. I. Katsnelson, Role of direct exchange and Dzyaloshinskii-Moriya interactions in magnetic properties of graphene derivatives: C_2F and C_2H, Phys. Rev. B **94**, 214411 (2016).

[28] Q. Wu, Y. Zhang, Q. Zhou, J. Wang, and X. C. Zeng, Transition-Metal dihydride monolayers: A new family of two-dimensional ferromagnetic materials with intrinsic room-temperature half-metallicity, J. Phys. Chem. Lett. **9**, 4260 (2018).

[29] S. Zhang, Y. Li, T. Zhao, and Q. Wang, Robust ferromagnetism in monolayer chromium nitride, Sci. Rep. **4**, 5241 (2014).

[30] A. V. Kuklin, A. A. Kuzubov, E. A. Kovaleva, N. S. Mikhaleva, F. N. Tomilin, H. Lee, and P. V. Avramov, Two-dimensional hexagonal CrN with promising magnetic and optical properties: A theoretical prediction, Nanoscale **9**, 621 (2017).

[31] Z. Zhu and D. Tománek, Semiconducting Layered Blue Phosphorus: A Computational Study, Phys. Rev. Lett. **112**, 176802 (2014).

[32] Y. Aierken, D. Çakır, C. Sevik, and F. M. Peeters, Thermal properties of black and blue phosphorenes from a first-principles quasiharmonic approach, Phys. Rev. B **92**, 081408 (2015).

[33] J. L. Zhang, S. Zhao, C. Han, Z. Wang, S. Zhong, S. Sun, R. Guo, X. Zhou, C. D. Gu, K. D. Yuan, Z. Li, and W. Chen, Epitaxial growth of single layer blue phosphorus: A new phase of two-dimensional phosphorus, Nano Lett. **16**, 4903 (2016).

[34] J. Zeng, P. Cui, and Z. Zhang, Half Layer by Half Layer Growth of a Blue Phosphorene Monolayer on a GaN(001) Substrate, Phys. Rev. Lett. **118**, 046101 (2017).

[35] J.-P. Xu, J.-Q. Zhang, H. Tian, H. Xu, W. Ho, and M. Xie, One-dimensional phosphorus chain and two-dimensional blue phosphorene grown on au(111) by molecular-beam epitaxy, Phys. Rev. Mater. **1**, 061002 (2017).

[36] P. E. Blöchl, Projector augmented-wave method, Phys. Rev. B **50**, 17953 (1994).

[37] G. Kresse and D. Joubert, From ultrasoft pseudopotentials to the projector augmented-wave method, Phys. Rev. B **59**, 1758 (1999).

[38] G. Kresse and J. Furthmüller, Efficiency of ab-initio total energy calculations for metals and semiconductors using a plane-wave basis set, Comput. Mater. Sci. **6**, 15 (1996).

[39] G. Kresse and J. Furthmüller, Efficient iterative schemes for *ab initio* total-energy calculations using a plane-wave basis set, Phys. Rev. B **54**, 11169 (1996).

[40] J. P. Perdew, K. Burke, and M. Ernzerhof, Generalized Gradient Approximation Made Simple, Phys. Rev. Lett. **77**, 3865 (1996).

[41] V. I. Anisimov, F. Aryasetiawan, and A. I. Lichtenstein, First-principles calculations of the electronic structure and spectra of strongly correlated systems: The LDA+U method, J. Phys.: Cond. Matter **9**, 767 (1997).

[42] S. L. Dudarev, G. A. Botton, S. Y. Savrasov, C. J. Humphreys, and A. P. Sutton, Electron-energy-loss spectra and the structural stability of nickel oxide: An LSDA+U study, Phys. Rev. B **57**, 1505 (1998).

[43] H. J. Monkhorst and J. D. Pack, Special points for Brillouin-zone integrations, Phys. Rev. B **13**, 5188 (1976).

[44] S. Grimme, Semi empirical GGA-type density functional constructed with a long-range dispersion correction, J. Comp. Chem. **27**, 1787 (2006).

[45] J. Klimes, D. R. Bowler, and A. Michaelides, Van der Waals density functionals applied to solids, Phys. Rev. B **83**, 195131 (2011).

[46] J. Klimes, D. R. Bowler, and A. Michaelides, Chemical accuracy for the van der Waals density functional, J. Phys.: Cond. Matter **22**, 022201 (2009).

[47] See Supplemental Material at http://link.aps.org/supplemental/10.1103/PhysRevApplied.11.064015 for results obtained using different exchange-correlation functionals.

[48] A. Togo, L. Chaput, and I. Tanaka, Distributions of phonon lifetimes in Brillouin zones, Phys. Rev. B **91**, 094306 (2015).

[49] G. Pizzi, D. Volja, B. Kozinsky, M. Fornari, and N. Marzari, BOLTZWANN: A code for the evaluation of thermoelectric and electronic transport properties with a maximally-localized Wannier functions basis, Comp. Phys. Commun. **185**, 422 (2014).

[50] A. A. Mostofi, J. R. Yates, Y.-S. Lee, I. Souza, D. Vanderbilt, and N. Marzari, wannier90: A tool for obtaining maximally-localised Wannier functions, Comp. Phys. Commun. **178**, 685 (2008).

[51] N. Marzari and D. Vanderbilt, Maximally localized generalized Wannier functions for composite energy bands, Phys. Rev. B **56**, 12847 (1997).

[52] N. Marzari, A. A. Mostofi, J. R. Yates, I. Souza, and D. Vanderbilt, Maximally localized Wannier functions: Theory and applications, Rev. Mod. Phys. **84**, 1419 (2012).

[53] J. L. Lado and J. Fernández-Rossier, On the origin of magnetic anisotropy in two dimensional CrI_3, 2D Mater. **4**, 035002 (2017).

[54] W. Li, L. Sun, J. Qi, P. Jarillo-Herrero, M. Dincă, and J. Li, High temperature ferromagnetism in π-conjugated two-dimensional metal-organic frameworks, Chem. Sci. **8**, 2859 (2017).

[55] J. Rusz, I. Turek, and M. Diviš, Random-phase approximation for critical temperatures of collinear magnets with multiple sublattices: GdX compounds (X = Mg,Rh,Ni,Pd), Phys. Rev. B **71**, 174408 (2005).

[56] M. Hortamani, L. Sandratskii, P. Kratzer, I. Mertig, and M. Scheffler, Exchange interactions and critical temperature of bulk and thin films of MnSi: A density functional theory study, Phys. Rev. B **78**, 104402 (2008).

[57] K. Momma and F. Izumi, VESTA 3 for three-dimensional visualization of crystal, volumetric and morphology data, J. Appl. Cryst. **44**, 1272 (2011).

[58] L. Webster, L. Liang, and J.-A. Yan, Distinct spin-lattice and spin-phonon interactions in monolayer magnetic CrI_3, Phys. Chem. Chem. Phys. **20**, 23546 (2018).

[59] G. Binasch, P. Grünberg, F. Saurenbach, and W. Zinn, Enhanced magnetoresistance in layered magnetic structures with antiferromagnetic interlayer exchange, Phys. Rev. B **39**, 4828 (1989).

[60] V. F. Gantmakher and Y. B. Levinson, in *Modern Problems in Condensed Matter Sciences*, edited by V. M. Agranovich and A. A. Maradudin (Elsevier Science Publishers, Amsterdam, 1987), Vol. 19, Chap. 13.